


Received May 6, 2019, accepted May 25, 2019, date of publication May 28, 2019, date of current version June 26, 2019.

Digital Object Identifier 10.1109/ACCESS.2019.2919624

# Raster-Based Background Filtering for Roadside LiDAR Data

BIN LV<sup>1</sup>, HAO XU<sup>2</sup>, JIANQING WU<sup>1</sup><sup>2</sup>, YUAN TIAN<sup>2</sup>, AND CHANGWEI YUAN<sup>3</sup>

<sup>1</sup>School of Traffic and Transportation, Lanzhou Jiaotong University, Lanzhou 730070, China

<sup>2</sup>Department of Civil and Environmental Engineering, University of Nevada, Reno, NV 89557, USA

<sup>3</sup>School of Economics and Management, Chang' An University, Xi'an 710064, China

Corresponding authors: Bin Lv (jdlbxx@mail.lzjtu.cn) and Jianqing Wu (jianqingwu2015@gmail.com)

This work was supported in part by the Natural Science Foundation of China under Grant 61463026 and Grant 61463027, in part by the Foundation of Hundred Youth Talents Training Program of Lanzhou Jiaotong University, in part by the Nevada Department of Transportation (NDOT) under Grant P224-14-803/TO #13, in part by the Fundamental Research Funds for the Central Universities under Grant 300102238614, and in part by the Ministry of Education of Humanities and Social Science under Grant 18YJAZH120.

**ABSTRACT** The roadside deployed light detecting and ranging (LiDAR) has been a solution to fill the data gap for the transition period from the unconnected-vehicles environment to the connected-vehicles system. For the roadside LiDAR system, background filtering is an initial but important step. This paper presented a raster-based method for background filtering with roadside LiDAR data. The proposed method contains four major parts: region of interest (ROI) selection, rasterization, background area detection, and background array generation. The location of the background points was stored in a 3D array. The performance of the raster-based method was tested with the data collected at different scenarios. The comparison to the state-of-the-art also confirmed the robustness of the proposed method.

**INDEX TERMS** Background filtering, roadside LiDAR, connected-vehicles.

## I. INTRODUCTION

The Light detecting and ranging (LiDAR) is originally a remote sensing method that uses light to measure the distance. LiDAR has recently become prevalent in transportation engineering, it can be used in such as asset data collections, traffic data collection, and so on [1]. The traditional LiDARs can be divided into two parts by the different types of installation: airborne LiDAR, mobile LiDAR, and terrestrial LiDAR. The airborne LiDAR is usually installed on a helicopter or drone, which can be used for digital terrain models extraction, city 3D reconstruction, and flood control [2]–[5]. The on-board LiDAR, also called mobile-LiDAR, has been applied for automated extraction of road markings [6], [7], sidewalk detection [8], pedestrian identification [9], road boundary detection [10], and vehicle tracking [11] on autonomous vehicles [12]. In recent years, the concept of the roadside deployment of the LiDAR gradually appeared, namely, the roadside LiDAR. It is also called stationary LiDAR or side-fire LiDAR refers to the LiDAR installed in a fixed location temporarily or permanently [13].

One major application for deploying the roadside LiDAR is to serve the connected-vehicle technology [14]. Connected vehicles can provide extended distance for drivers

(or autonomous systems) to “see” around corners or “through” other vehicles via the real-time communication of vehicle-to-vehicle and vehicle-to-infrastructure. Therefore, safety threats and traffic changes require to be perceived earlier in a connected-vehicle environment [15]. The full benefits of connected-vehicle systems need all vehicles to be equipped with connected-vehicle devices and broadcast high-resolution micro traffic data (HRMTD) in real time. However, most of the vehicles on the roads are not connected with each other currently. The mixed traffic with connected-vehicles and unconnected-vehicles will exist in the next decades or even longer [14]. How to obtain HRMTD, meaning second-by-second (or at a higher frequency) of those unconnected road users and broadcast to the connected-vehicles is a challenge for transportation engineering [16]. The roadside LiDAR presents a good solution to collect the HRMTD of all road users on the road. The 360-degree rotating LiDAR is able to detect the objects with a 360-degree horizontal field of view (FOV). It can work in both days and nights regardless of the influence of light condition. The LiDAR can detect the surrounding objects then provide a cloud of points with the XYZ coordinates in high frequency (usually 5~20 Hz, varies from different LiDAR manufacturers). With LiDAR sensors at intersections and along roads, HRMTD of each individual road user can be extracted and shared with other roadway users by wireless communication technologies [17].

The associate editor coordinating the review of this manuscript and approving it for publication was Nuno Garcia.

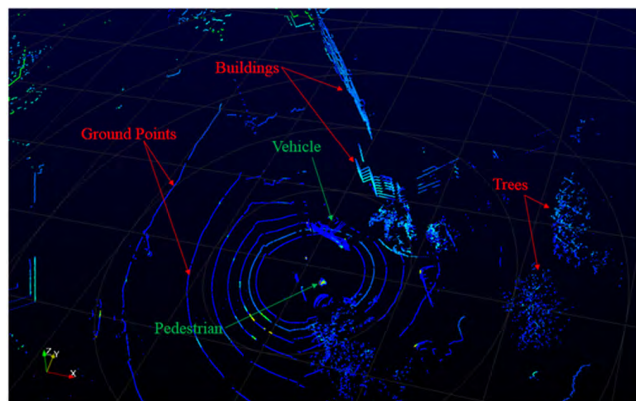


**FIGURE 1.** Point clouds from raw LiDAR data.

Figure 1 shows an example of a roadside LiDAR data collection frame. The roadside LiDAR can detect all the objects in its scanned range, including ground points, buildings, trees, vehicles, and pedestrians.

To extract the HRMTD from the roadside LiDAR, the background points, including buildings, trees and ground points, need to be excluded firstly since the objects of interest of connected-vehicles are road users, rather than background points. This step is usually named background filtering in transportation. The background filtering is the basic step for processing the raw LiDAR data. The accuracy of the object clustering and tracking rely heavily on the accuracy of background filtering. The background points can be divided into two camps: static points and dynamic points. The static background points refer to the points that are relatively fixed in different timestamps, such as buildings and ground points. The dynamic background points refer to the points those may move within a limited distance in different timestamps, such as tree branches. The purpose of the background filtering is to keep the objects of interest as much as possible and to exclude the other irrelevant points (both static background points and dynamic background points) at the same time. For an automatic procedure, the essence of the background filtering issue is to train a classifier to distinguish background points and non-background points. However, the challenge is that the positions of the background points are not fixed in the roadside LiDAR data due to the occlusion issue or vibration of the LiDAR sensor. There have been a bunch of background filtering algorithms developed for airborne LiDAR and on-board LiDAR. For survey using airborne LiDAR data, the background points refer to ground surface. The ground surface detection has been relatively mature since several methods, such as Minimum Description Length (MDL) models, constrained spline functions, active contour models like snakes or geometrical thresholds for elevation differences, have been developed for ground surface detection [18]. Levinson *et al.* [19] used the depth information to exclude ground points for onboard LiDAR considering the fixed height of the LiDAR above the ground. This approach works well when the terrain is flat. Ai and Tsai

also used the height information to distinguish the object of interest and other background points [8]. For airborne LiDAR and mobile LiDAR, the vegetation and buildings may be objects of interest. But for roadside LiDAR serving connected vehicles, vegetation and buildings are considered as background points and should be excluded during the background filtering step. Therefore, those above-mentioned background filtering algorithms could not be directly used for the roadside LiDAR. Some early studies related to background filtering for roadside LiDAR have been found in the literature. Ibisch *et al.* [20] proposed a 2D grid-based approach to separate the vehicles and background points for the roadside LiDAR. Space was divided into quadratic cells. Each cell can be identified as “occupied” or “non-occupied” based on the LiDAR rays. This grid-based method was designed for vehicle detection in a parking garage, which means only static background points can be excluded. Tarko *et al.* [21] considered ground surface as background points and used the height information to exclude the ground points. Lee and Coifman [22] considered one frame without any road user as a reference frame for background filtering. Any points had the same position in the reference frame were identified as background points. Again, this method can only exclude static background points. More recently, Zhang *et al.* [23] developed a background filtering approach, named as data association (DA), for roadside LiDAR. They assumed that the dynamic background points had a relatively fixed motion track during different frames. Then by giving a threshold, the dynamic background points could be identified and excluded. However, this method required a manual selection of an initial frame. The authors also have several studies related to background filtering. In a very early study [17], the authors raised up a density-based background filtering algorithm in 3D space (3D-DSF). Instead of finding a fix position for background points, the 3D-DSF divides the space into small cubes with an equal side length. Each cube can be identified as a background cube or non-background cube. By aggregating multiple frames into one space, those background cube contains more points than those non-background points. By giving a pre-defined threshold (TD), those background cubes can be identified. Any point found in those background cubes were considered as background points and excluded from the space. Later in [24], the 3D-DSF were improved by giving a dynamic TD for different scenarios. The TD is influenced by two factors: distance to LiDAR and the existence of moving road users on the road. Dynamic values were provided for the areas with different distances to LiDAR and for different scenarios with or without moving road users. For the details of 3D-DSF, we refer the readers to [24]. Our developed 3D-DSF algorithm has been widely used for different applications of roadside LiDAR data processing, including lane identification, vehicle tracking, pedestrian detection, wildlife detection, vehicle classification, and safety assessment [25]–[33]. The major limitation for the 3D-DSF is that the accuracy can be dramatically reduced if vehicles stopped at intersections for a while [24]. For example, if one

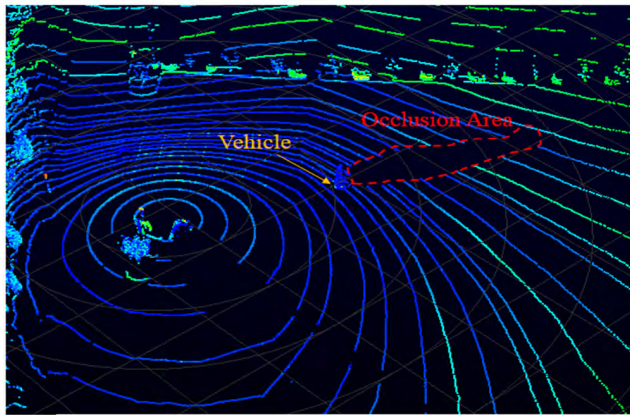


FIGURE 2. Occlusion issue.

vehicle stopped at the intersection waiting for the traffic signal, the algorithm can easily consider the stopped vehicle as the background points since it did not move for a relatively long time. Another issue for 3D-DSF is the object occlusion problem. When one vehicle exists in the space, an occlusion area is created inevitably [14]. As a result, the number of points becomes zero in the cubes within the blocking area. Figure 2 illustrates the issue.

## II. ROADSIDE LIDAR FOR HRMTD DATA COLLECTION

The HRMTD can be collected by conventional probe vehicles or connected vehicles with the GPS logging function [34]. However, probe vehicles or a low number of connected vehicles provide only sample data of the traffic fleet on roads, while the connected-vehicle applications need the data of all road users. The traditional traffic sensors such as loop detectors and cameras mainly provide macro traffic data such as traffic flow rates, average speeds (or spot speeds), and occupancy [35]. The performance of cameras can be greatly influenced by light conditions [36]. The most common approach for real-time traffic data collection is using active sensors such as radar-based method or Light Detection and Ranging (LiDAR)-based method. Radar has been widely used for object detection on autonomous vehicles [37], [38]. The practice shows that radar can detect the object in a specific range due to a limited horizontal field of view [39]. A LiDAR can transmit and receives electromagnetic radiation at a higher frequency than radar [40]. The LiDAR can also provide a longer detection range than the other types of sensors [41]. Either airborne LiDAR or on-board LiDAR can only provide HRMTD of partial road users. As mentioned before, the connected-vehicles require HRMTD of each individual road user. The roadside deployment of LiDAR provides a solution for HRMTD collection of all road users. The major reason why LiDAR sensors were not widely used for roadside applications was due to the high historical price [28]. Fortunately, the price of LiDAR has dropped to a thousand-dollar level in recent years. For example, the unit price of VLP-32c used to be more than \$50,000. But in 2018, the authors can buy the VLP-32c with \$3,999 per unit from

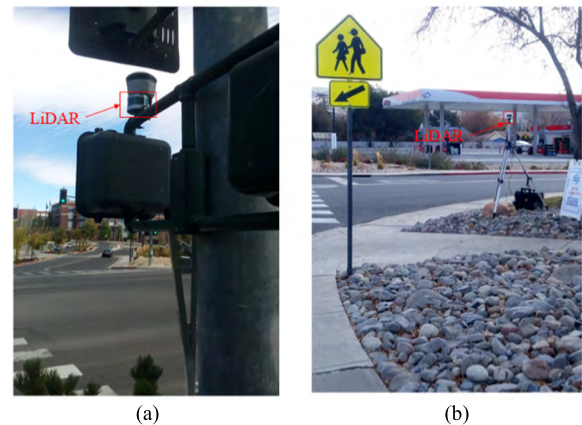


FIGURE 3. LiDAR installation. (a) Permanent installation. (b) Temporary installation.

TABLE 1. Major features of VLP-32c and VLP-16.

|   | VLP-32c                             | VLP-16                            |
|---|-------------------------------------|-----------------------------------|
| Horizontal Field of View                | 360°                                | 360°                              |
| Rotation Rate                           | 5 Hz – 20 Hz                        | 5 Hz – 20 Hz                      |
| Vertical Field of View                  | 40° (+15° to -25°)                  | 30° (± 15°)                       |
| Detection Range                         | Up to 200 meters                    | Up to 100 meters                  |
| Channels                                | 32                                  | 16                                |
| Angular Resolution (Vertical)           | 0.33°                               | 2°                                |
| Angular Resolution (Horizontal/Azimuth) | 0.1° to 0.4°                        | 0.2°                              |
| Return Models                           | Single or dual return               | Strongest, last or dual return    |
| Wave Length                             | 903 nm                              | 903 nm                            |
| Power Consumption                       | 10 Watt (Typical)                   | 8 Watt (Typical)                  |
| Accuracy                                | ±3 cm (Typical)                     | ±3 cm (Typical)                   |
| Operation Temperature                   | -20°C to +60°C                      | -10 °C to +60 °C                  |
| Storage Temperature                     | -40°C to +85°C                      | -40 °C to +105 °C                 |
| Weight                                  | 925 g                               | 803 g                             |
| Dimensions                              | 103 mm Diameter *<br>86.9 mm Height | 103 mm Diameter<br>* 72 mm Height |

the vendor. Although the price of LiDAR is still a little higher compared to the other traditional sensors currently, it's time to do pilot studies about the data processing algorithms for the roadside LiDAR. The LiDAR can be installed on the roadside permanently or temporarily, depending on different purposes [23]. Figure 2 shows two examples of roadside LiDAR installation. The LiDAR can be installed on a roadside infrastructure, such as on the top of a pedestrian signal in Figure 3 (a), for permanent HRMTD collection. It can also be installed on a tripod to collect short-term traffic data, as shown in Figure 3 (b). The height of the LiDAR depends on the vertical FOV. For VLP-16 with a 30-degree vertical FOV, the recommended height is 7 ft~ 9 ft above the ground [25].

Our proposed background filtering algorithm can work for any rotating LiDAR sensor as long as the XYZ coordinates are reported. Though the algorithm does not rely on any specific brand of LiDAR sensor, we tested the algorithm using VLP-16 and VLP-32c. The major features of VLP-16 and VLP-32 are documented in Table 1.



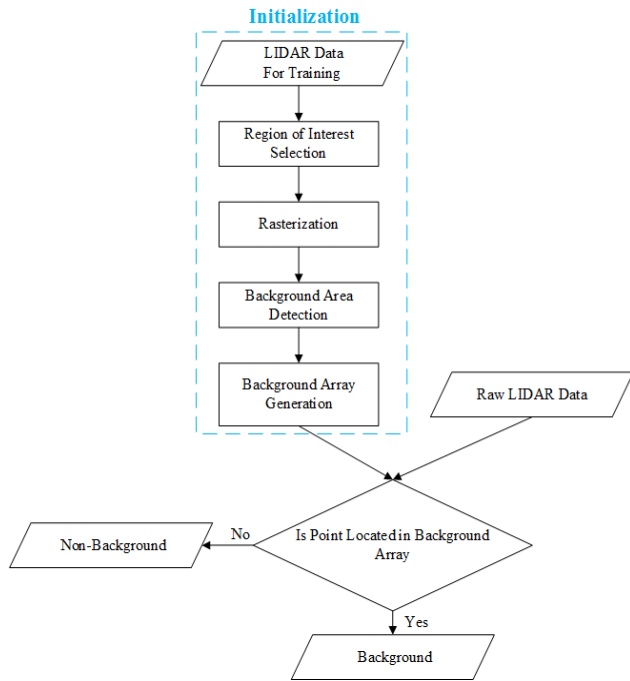


FIGURE 4. Flow chart of RA.

### III. RASTER-BASED ALGORITHM (RA)

The structure of RA is illustrated in Figure 4. The RA contains four major parts: region of interest selection, rasterization, background area detection, and background array generation. The locations of the background are stored in an array. For the roadside LiDAR data, any point located in the array is considered as background.

#### A. REGION OF INTEREST SELECTION

Assume the max vertical angle is  $\theta$  and the effective range of detection in the horizontal direction is  $d$ , the max effective vertical detecting height-  $h$  can be calculated with Equation 1.

$$h = d * \tan\theta \tag{1}$$

The boundary of the region of interest (ROI) in vertical direction should be within  $\pm h$ . In practice, the height of the roadside LiDAR is usually installed in a height- $H$  (usually 7ft~9ft) above the ground. Under this situation, the vertical range is from  $-H$  to  $H+h$ . Any points out of the boundary in Equation 2 can be directly excluded from the space. Where  $X$  and  $Y$  are the x-axis value and y-axis value of points, respectively. Excluding points out of ROI can reduce computation load for the following data processing steps [42].

$$ROI = \left( \begin{array}{l} -d \leq X \leq d \\ -H \leq Y \leq H + h \end{array} \right) \tag{2}$$

#### B. RASTERIZATION

As mentioned before, the locations of the background points are not fixed in different frames, even though the location of the roadside LiDAR is relatively fixed. Therefore, directly identifying each background points in each

frame is almost unrealistic. But the offset of those background points was small in general [31]. Motivated by the rasterization (converting vector to raster) in the imaging technology [43]–[45], the LiDAR points in the space were firstly rasterized into small cubes instead of directly excluding the background points. The location of each cube can be stored in a  $M * M * N$  array.

$$M = 2d/L \tag{3}$$

$$N = (2H + h)/L \tag{4}$$

where  $d$  is the horizontal detection range,  $L$  is the side Length of the cube,  $H$  is the height of the roadside LiDAR from the ground, and  $h$  is the max effective vertical detecting height of LiDAR.

The rasterization is illustrated as follows. For each frame, the 3D space in ROI was chopped into small cubes with the same side length- $L$ , which is similar to 3D-DSF. The selection of side length- $L$  is critical, which can influence the accuracy and computational load of the  $M * M * N$  array generation. There are some tradeoffs for the selection of  $L$ . A higher value of  $L$  can increase the computational speed, but at the same time, will decrease the accuracy of background filtering (one cube may contain both background points and non-background points). A lower value of side length can enhance the accuracy of background filtering but will aggravate the computational load of the computer. In general, the side length of the cube should be larger than the resolution error of the LiDAR. The recommended side length is 0.1 m considering the computational load and the accuracy [24]. After space is rasterized, the focus of background filtering changed to identify the cubes representing background.

#### C. BACKGROUND AREA DETECTION

For one frame, without comparing to other frames, it is difficult to know which cube represents background when there are moving objects in the space. The DA method developed by Zhang *et al.* [23] manually selects one frame without any moving objects in the space as a reference frame (RF). Then any cube contains the points in the RF can be identified as the background cubes. The issue for this method is that this method could not exclude the dynamic background points effectively. Furthermore, for the road with heavy traffic volume, it is even unrealistic to manually find a frame without any moving objects. Therefore, the algorithm should focus on identifying the background locations in multiple frames, instead of in one frame. Tarko *et al.* [42] by analyzing the distance change of LiDAR points collected in 15 minutes to identify the background points. Distance readings recorded by each laser at each angle were grouped separately. The existence of moving objects can generate a shorter distance. Then any points with a distance less than a pre-defined threshold will be considered as the background points. This method requires the frames with low traffic volume as the input. When the traffic volume is heavy in the aggregated frames, the accuracy of this algorithm can be dramatically reduced.



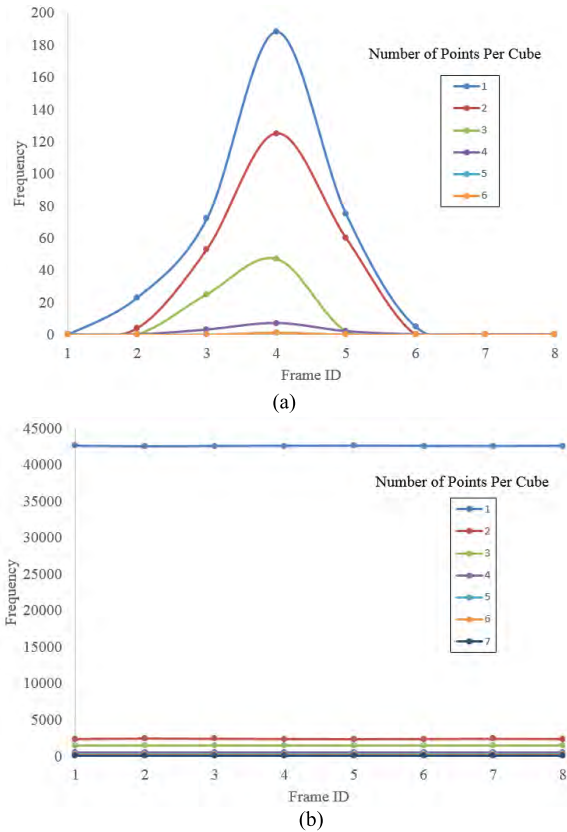


FIGURE 5. Point density distribution. (a) Non-background cubes with a moving vehicle passing. (b) Background cubes.

Similar to Tarko et al.’s method [42], 3D-DSF also considered the point distribution in multiple frames. A threshold of point density per cube is defined to distinguish background cubes and non-background cubes. The challenge of identifying background cubes under heavy traffic volume (especially when the vehicle stopped at intersections) is left unsolved. Instead of focusing the value of point density in aggregated frames like 3D-DSF, the proposed RA algorithm used the change of the point density in multiple frames to identify those background cubes. The idea of RA is that though it is impossible to identify all the background area in one frame, identifying a partial background area is feasible. It is assumed that the non-background points will move in a relatively long time. For example, as long as the investigating time is longer than the red signal time at the intersection, the vehicles should move after red signal time or before the red signal starts, if spillback is not considered. Then by aggregating the background areas in different frames, the whole background area can be identified. The challenge here is how to identify background parts in each frame. An automatic background identification algorithm in each frame is proposed as follows.

When one object enters the detection range of the LiDAR, compared to the previous frame, the point density of the cubes where the object occupies increases. At the same time, the point density of the occlusion area (if exist) decreases. For the other parts, the point density does not change. Figure 5 shows an example of the change of background point density

TABLE 2. Frequency of the change of point density in different frames.

|                      | Frame ID | Change of Number of Points in each Cube |     |    |    |
|----------------------|----------|---|-----|----|----|
|                      |          | 1                                       | 2   | 3  | 4  |
| Non-background Cubes | 1        | NA                                      | NA  | NA | NA |
|                      | 2        | 23                                      | 4   | 0  | 0  |
|                      | 3        | 59                                      | 49  | 21 | 0  |
|                      | 4        | 138                                     | 103 | 8  | 1  |
|                      | 5        | 144                                     | 109 | 9  | 1  |
|                      | 6        | 70                                      | 60  | 4  | 0  |
|                      | 7        | 5                                       | 0   | 0  | 0  |
|                      | 8        | 0                                       | 0   | 0  | 0  |
|                      | Frame ID | Change of Number of Points in each Cube |     |    |    |
|                      |          | 1                                       | 2   | 3  | 4  |
| Background Cubes     | 1        | NA                                      | NA  | NA | NA |
|                      | 2        | 1,015                                   | 75  | 0  | 0  |
|                      | 3        | 964                                     | 84  | 0  | 0  |
|                      | 4        | 1,001                                   | 81  | 0  | 0  |
|                      | 5        | 945                                     | 69  | 0  | 0  |
|                      | 6        | 992                                     | 79  | 0  | 0  |
|                      | 7        | 10,003                                  | 56  | 0  | 0  |
|                      | 8        | 987                                     | 63  | 0  | 0  |

TABLE 3. Non-background cube identification.

|   |   |
|---|---|
| 1 | begin   |
| 2 | if $\min(Na_i) = 0$ ; N is the point density, a is the Cube ID, and i is the Frame ID |
| 3 | a is suspect non-background cube;   |
| 4 | else if $\min(Na) > 0$ ;  |
| 5 | if $N_{a(i+1)} - N_{a_i} > 2$ ;   |
| 6 | a is suspect non-background cube;   |
| 7 | end   |
| 8 | end   |

in different frames with VLP-32c. In Figure 5 (a), a vehicle passed the non-background cubes from Frame 1 to Frame 7. The change of point density was obvious for different frames. The trend of the point density fits like a normal distribution. When there was no moving object in the non-background cubes, the point density was zero. The point density increases when the vehicle enters the cubes. The density decreased after reaching a peak value. When the vehicle passed all the cubes (at Frame 7), the point density of all the cubes went back to zero. Figure 5 (b) shows the point density distribution for those background cubes. For those background cubes, the point density change between different frames was tiny since there were no moving objects passing them.

Table 2 further illustrates the frequency of the change of point density in different frames.

It is clearly shown that the change of point density (3 and 4) in two adjacent frames only occurred in non-background cubes. The change interval of all background cubes is less than or equal to 2. Therefore, the following criteria can be used to distinguish background cube and non-background cube.

With this criterion in Table 3, the background cubes and suspect non-background cubes can be divided. Here the term

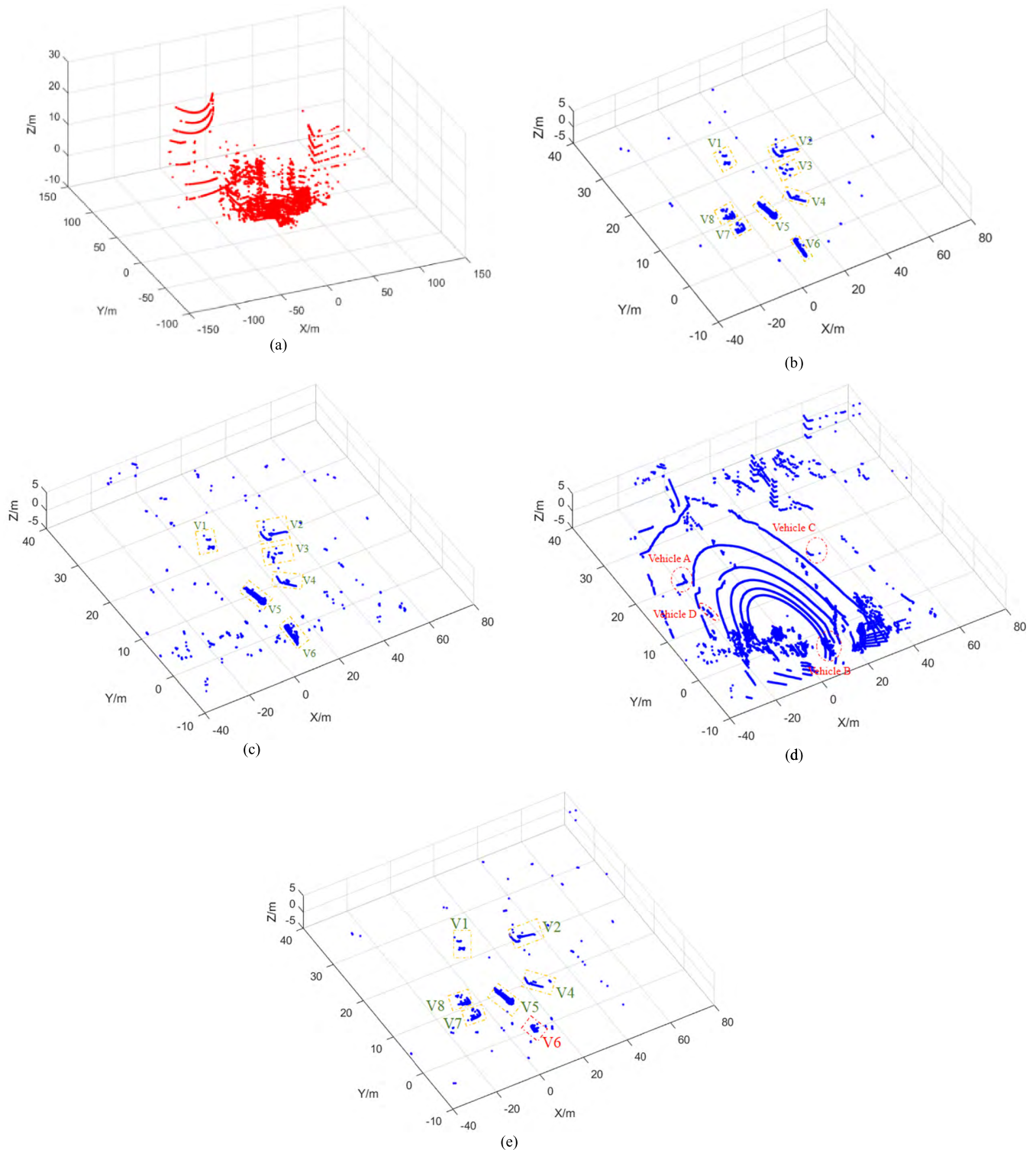


**FIGURE 6.** Background filtering at N Virginia St@15th St. (a) Raw LiDAR Points. (b) RA Result. (c) 3D-DSF Result. (d) Reference Frame for DA. (e) DA Results.

“suspect non-background cube” is used since some suspect non-background cubes may be background cubes. Due to the occlusion issue, the feature of the background cubes in the occluded part may also meet the criteria. For the occlusion part, when they are occluded by the moving objects, the point density goes to zero. If the point density of the background

is high, when the occlusion disappears, the change of the point density can be also larger than 2. Therefore, further efforts need to be conducted to distinguish non-background cubes and background cubes in the suspect non-background cubes. For the occlusion part, we assumed that in a relatively long time (15 minutes-9000 frames if the rotating frequency

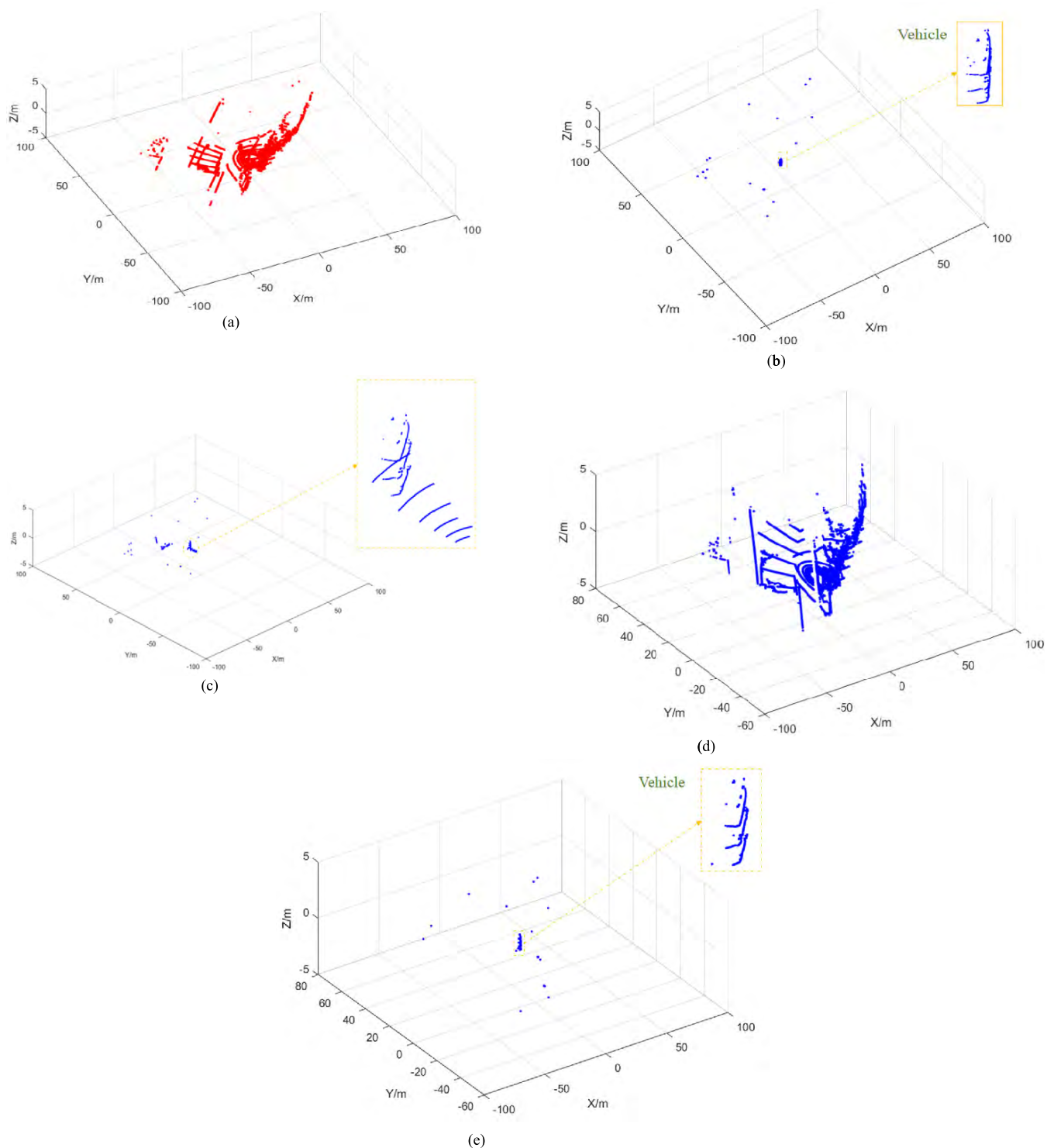


**FIGURE 7.** Background filtering at 180 in Elko. (a) Raw LiDAR points. (b) RA result. (c) 3D-DSF result. (d) Reference frame for DA. (e) DA results.

is 10 HZ), the occlusion issue only occurred in a low percentage. In the number of frames when the cube has a zero point density can be recorded as  $NCD_0$  and the number of frames when the cube has a positive point density can be recorded as  $NCD_+$ . If  $NCD_0 > NCD_+$ , this cube is considered as background. Otherwise, this is a non-background cube.

#### IV. CASE STUDY

To evaluate the performance of the proposed method, the raster-based algorithm is compared to the state-of-the-art. Two methods: 3D-DSF and Data Association (DA) [23] are selected to represent the newest background filtering algorithms for roadside LiDAR data. The performance of the



three methods was compared by processing the LiDAR data collected at different sites.

### A. INTERSECTION WITH HEAVY TRAFFIC VOLUME

The intersection-N Virginia St@ 15th Street is a signalized intersection in Reno, Nevada which was selected as the heavy traffic volume testbed. The annual average daily traffic (AADT) on N Virginia St is 11000 vehicles. During peak hours, even every frame have vehicles on the road. For 3D-DSF, 1500 frames (150 seconds) were used for training the background. An initial frame is selected manually as a reference frame for DA. Figure 6 shows the before-and-after background filtering for the three different methods. The data were collected during the peak hour. In the frame, there were 8 vehicles (V1~V8) in the space. As shown in Figure 6 (b), most background points were excluded by RA and all vehicles were left in the space. However, for 3D-DSF, only 6 vehicles (V1, V2, V3, V4, V5, and V6) can be seen after background filtering, as shown in Figure 6 (c). V7 and V8 were missing owing to they stopped at the intersection. There were more points left in the space using 3D-DSF compared to RA. The frame with four vehicles (Vehicle A~D) in Figure 6 (d) was selected as the reference frame for DA. There were seven vehicles left in the frame after DA filtering. V3 was missing since its location coincided with the location of Vehicle C in the reference frame. Furthermore, the length of V6 was shorter compared to the results of the other two methods since there were some overlap between the location of V6 and Vehicle B. Figure 6 shows that for background filtering at intersections with heavy traffic volume, RA performs best among the three investigated methods.

### B. ROBUSTNESS TO PACKET LOSS

Packet loss refers to the situation that parts of points cloud are missing in the LiDAR data. Packet loss is usually due to the instability of the LiDAR or the communication issue between the LiDAR and the computer. The location of missing packet varies in different frames. Background filtering for the LiDAR data with packet loss can be a challenge. The freeway-I80 near Elko, Nevada were selected for background filtering since the collected data contains a lot of packet loss. Figure 7 shows an example of background filtering with packet loss using three different methods. Since this is a rural freeway, the traffic volume is low, it is possible to identify a frame without any vehicle and without packet loss issue at the same time, as shown in Figure 7(d). Figure 7 (b) and Figure 7 (e) shows the performance of RA and DA is similar. Most background points were excluded and one vehicle left in the space using RA and DA. However, for 3D-DSF, even the vehicle was also left in the space, a lot of ground points were also left around the vehicle. This is caused by the packet loss in the aggregated frames at this location. The high percentage of packet loss at this location decreased the point density in the cubes and the point density of background cubes could not meet the threshold in 3D-DSF. As a result, the background cubes were misclassified as non-background cubes.

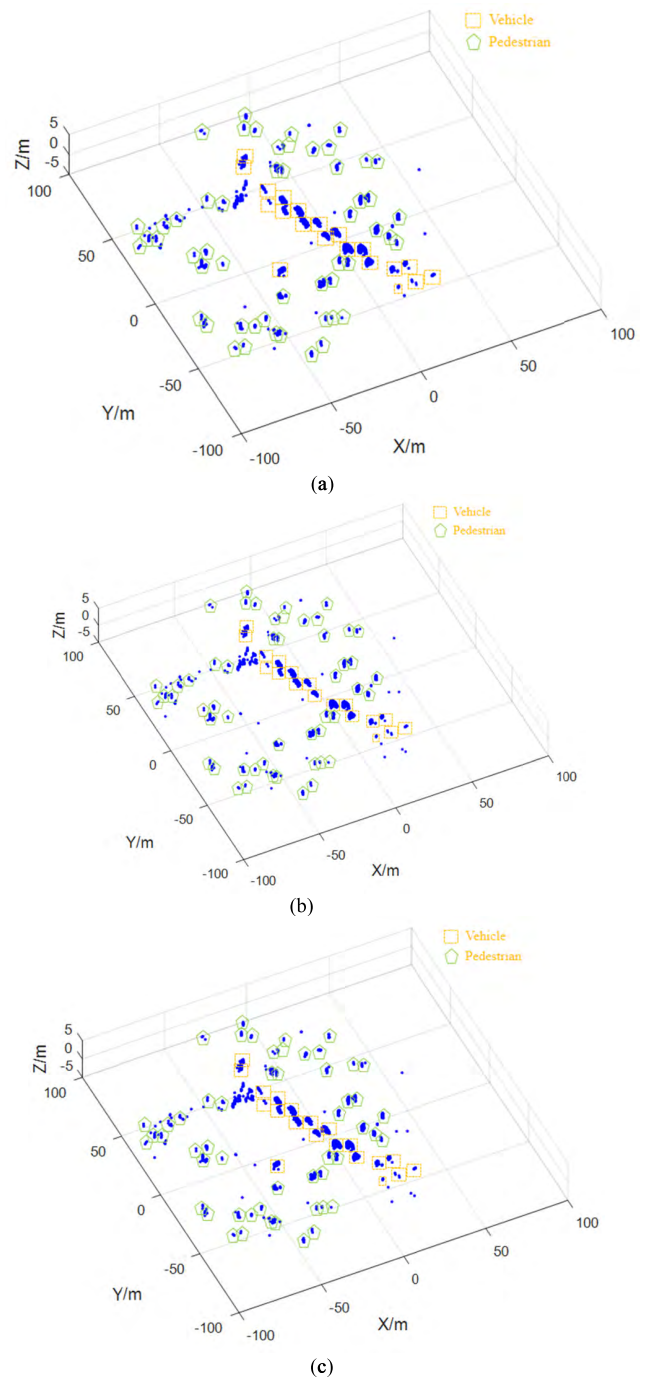


**FIGURE 8.** Background filtering at baring Blvd.(a) RA result. (b) 3D-DSF result. (c) DA result.

Therefore, RA still performs best compared to the state-of-the-art methods.

### C. MULTIPLE TRAFFIC USERS

Other than vehicles, pedestrians are another major road users on the road. Pedestrians should be kept in the space after background filtering. Baring Blvd is selected as the multiple traffic users case in Northeastern Reno. Since it is close to Reed High School, a lot of students walk along or cross Baring Blvd during lunch time. Figure 8 shows the results

**TABLE 4. Quantitative analysis of background filtering.**

| Location                      | LiDAR   | Background points | Number of vehicles* | Number of pedestrians | Background points (after) | Number of vehicles (after) | Number of pedestrians (after) | Percentage of background filtering | Percentage of excluded vehicles | Percentage of excluded pedestrians |
|-------------------------------|---------|-------------------|---------------------|-----------------------|---------------------------|----------------------------|-------------------------------|------------------------------------|---------------------------------|------------------------------------|
| Virginia@ 15 <sup>th</sup> St | VLP-16  | 358,460           | 119                 | None                  | RA                        | 659                        | 119                           | 99.8%                              | 0%                              | None                               |
|                               |         |                   |                     |                       | 3D-DSF                    | 891                        | 110                           | 99.7%                              | 8.2%                            |                                    |
|                               |         |                   |                     |                       | DA                        | 751                        | 112                           | 99.8%                              | 5.9%                            |                                    |
|                               |         |                   |                     |                       | RA                        | 340                        | 8                             | 99.9%                              | 0%                              | None                               |
| I80                           | VLP-16  | 338,203           | 8                   | None                  | 3D-DSF                    | 12,620                     | 8                             | 96.3%                              | 0%                              |                                    |
|                               |         |                   |                     |                       | DA                        | 312                        | 8                             | 99.9%                              | 0%                              |                                    |
|                               |         |                   |                     |                       | RA                        | 8,791                      | 152                           | 98.5%                              | 0%                              | 1.1%                               |
|                               |         |                   |                     |                       | 3D-DSF                    | 9,562                      | 148                           | 98.4%                              | 2.6%                            | 2.3%                               |
| Baring Blvd                   | VLP-32c | 597,016           | 152                 | 439                   | DA                        | 8,972                      | 152                           | 98.5%                              | 0%                              | 1.6%                               |
|                               |         |                   |                     |                       | RA                        | 152                        | 434                           | 98.5%                              | 0%                              | 1.1%                               |
|                               |         |                   |                     |                       | 3D-DSF                    | 9,562                      | 148                           | 98.4%                              | 2.6%                            | 2.3%                               |

\*Note: The number of vehicles is the sum of number of vehicles in each frame

of background filtering at Baring Blvd using three different methods. The results of the three methods were similar. Both RA and DA can keep 53 pedestrians and 19 vehicles after background filtering, while 3D-DSF can keep 52 pedestrians and 18 vehicles in the space. Overall, all the three methods can handle the situation with mixed traffic road users.

#### D. QUANTITATIVE ANALYSIS

The quantitative comparison of the three methods is documented in Table 4. At each site, 20 frames were randomly selected for checking. For each frame, the background points and non-background points were manually identified. For the background points, the performance of the three methods is similar. The RA has a slightly higher accuracy than 3D-DSF and DA. All the three methods can exclude more than 98% of background points in the three sites. For the vehicle excluded percentage, 3D-DSF generates the highest error among the three methods, especially at the intersection. The accuracy of RA has the highest overall accuracy. For the computational load, 3D-DSF requires more than 25 minutes for initialization, while RA only requires 20 minutes (in general). The major difference for the use of computational load is that 3D-DSF needs to aggregate all the frames into one space and DA requires to manually select the reference frame, while RA does not require those steps. The platform used to run the three algorithms is a Dell desktop with i7-4900 CPU and 16 GB of RAM. For the real-time data processing, the time used to exclude background for each frame is 100 ms using RA, 100 ms using 3D-DSF, and 250 ms using DA, respectively. The limited time cost can guarantee RA exclude the background points in real-time for HRMTD collection.

#### V. CONCLUSION

This paper presents a raster-based algorithm for background filtering serving roadside LiDAR sensor. The proposed algorithm identifies the background cubes in the space by analyzing the change of point density per cube in different frames. The developed algorithm can guarantee the high accuracy of background filtering under heavy traffic volume and is

non-sensitive to stopped vehicles at intersections. The raster-based algorithm is also robust for packet-loss situations. Compared to the state-of-the-art, the proposed algorithm can provide higher accuracy but use less computational memory. The raster-based algorithm can be used for real-time background filtering for connected-vehicles and other transportation applications.

There are some further works regarding improving the accuracy of the raster-based algorithm. The selection of RA initialization time needs further investigation. The recommended value- 15 minutes is based on the authors' multiple testing using the data under different scenarios. An automatic procedure to select the initialization time with different traffic volume will be developed in the next step. The training data and testing data used only rotating LiDAR data. In theory, the raster-based algorithm can also work for solid LiDAR. But the authors' team did not have solid LiDAR data for testing. Testing the developed algorithm with solid LiDAR is expected to be conducted for future studies. The proposed algorithm could not exclude the hazes and snowflakes under severe weather (snowing or foggy weather) for the roadside LiDAR. Previous studies already showed that the performance of LiDAR decreased in the harsh environment [40], [46]. Integration of LiDAR, radar, and camera data may provide a robust detection system for real-time transportation practices. Therefore, how to use the data collected from other sensors to improve the accuracy of background filtering is also an interesting topic for the studies in the future.

#### REFERENCES

- [1] C. Ai and Y.-C. J. Tsai, "Critical assessment of an enhanced traffic sign detection method using mobile LiDAR and INS technologies," *J. Transp. Eng.*, vol. 141, no. 5, May 2014, Art. no. 04014096.
- [2] Y. Hu, "Automated extraction of digital terrain models, roads and buildings using airborne LiDAR data," M.S. thesis, Dept. Geomatics Eng., Univ. Calgary, Calgary, AB, Canada, 2003.
- [3] S. H. H. Nourzad and A. Pradhan, "Ensemble methods for binary classifications of airborne LiDAR data," *J. Comput. Civil Eng.*, vol. 28, no. 6, Nov. 2012, Art. no. 04014021.
- [4] J. Balsa-Barreiro, J. P. Vicent, and J. L. García, "Airborne light detection and ranging (LiDAR) point density analysis," *Sci. Res. Essays*, vol. 7, no. 33, pp. 3010–3019, 2012.

- [5] J. Balsa-Barreiro and J. L. Lerma, "A new methodology to estimate the discrete-return point density on airborne LiDAR surveys," *Int. J. Remote Sens.*, vol. 35, no. 4, pp. 1496–1510, Feb. 2014.
- [6] Y. Yu, J. Li, H. Guan, F. Jia, and C. Wang, "Learning hierarchical features for automated extraction of road markings from 3-D mobile LiDAR point clouds," *IEEE J. Sel. Topics Appl. Earth Observ. Remote Sens.*, vol. 8, no. 2, pp. 709–726, Feb. 2015.
- [7] H. Guan, J. Li, Y. Yu, Z. Ji, and C. Wang, "Using mobile LiDAR data for rapidly updating road markings," *IEEE Trans. Intell. Transp. Syst.*, vol. 16, no. 5, pp. 2457–2466, Oct. 2015.
- [8] C. Ai and Y. Tsai, "Automated sidewalk assessment method for americans with disabilities act compliance using three-dimensional mobile lidar," *Transp. Res. Rec., J. Transp. Res. Board.*, vol. 2542, no. 1, pp. 25–32, 2016.
- [9] T. Ogawa, H. Sakai, Y. Suzuki, K. Takagi, and K. Morikawa, "Pedestrian detection and tracking using in-vehicle lidar for automotive application," in *Proc. IEEE Intell. Vehicles Symp. (IV)*, Jun. 2011, pp. 734–739.
- [10] W. S. Wijesoma, K. R. S. Kodagoda, and A. P. Balasuriya, "Road-boundary detection and tracking using lidar sensing," *IEEE Trans. Robot. Autom.*, vol. 20, no. 3, pp. 456–464, Jun. 2004.
- [11] T. Miyasaka, Y. Ohama, and Y. Ninomiya, "Ego-motion estimation and moving object tracking using multi-layer lidar," in *Proc. IEEE Intell. Vehicles Symp.*, Jun. 2009, pp. 151–156.
- [12] C. Laugier and J. Chartre, "Intelligent perception and situation awareness for automated vehicles," GTC Eur., Amsterdam, The Netherlands, Tech. Rep. hal-01428547, Sep. 2016.
- [13] A. P. Tarko, K. B. Ariyur, M. A. Romero, V. K. Bandaru, and C. Liu, "Stationary LiDAR for traffic and safety applications—vehicle detection and tracking," Purdue Univ., Tech. Rep. FHWA/IN/JTRP-2016/24, 2016. doi: 10.5703/1288284316347.
- [14] J. Wu, "An automatic procedure for vehicle tracking with a roadside LiDAR sensor," *ITE J.-Inst. Transp. Eng.*, vol. 88, no. 11 pp. 32–37, Nov. 2018.
- [15] J. Wu, H. Xu, Y. Zheng, W. Liu, Y. Sun, R. Yue, and X. Song, "Driver behavior fault analysis on ramp-related crashes/near-crashes using SHRP 2 naturalistic driving study data," in *Proc. IEEE Int. Conf. Intell. Transp. Syst. (ITSC)*, Nov. 2018, pp. 2134–2139.
- [16] N. Lu, N. Cheng, N. Zhang, X. Shen, and J. W. Mark, "Connected vehicles: Solutions and challenges," *IEEE Internet things J.*, vol. 1, no. 4, pp. 289–299, Aug. 2014.
- [17] J. Wu, H. Xu, and J. Zheng, "Automatic background filtering and lane identification with roadside LiDAR data," in *Proc. IEEE 20th Int. Conf. Intell. Transp. Syst. (ITSC)*, Oct. 2017, pp. 1–6.
- [18] P. Axelsson, "Processing of laser scanner data—algorithms and applications," *ISPRS J. Photogram. Remote Sens.*, vol. 54, nos. 2-3, pp. 138–147, Jul. 1999.
- [19] J. Levinson, J. Askeland, J. Becker, J. Dolson, D. Held, S. Kammel, J. Z. Kolter, D. Langer, O. Pink, V. Pratt, M. Sokolsky, G. Stanek, D. Stavens, A. Teichman, M. Werling, and S. Thrun, "Towards fully autonomous driving: Systems and algorithms," in *Proc. IEEE Intell. Vehicles Symp. (IV)*, Jun. 2011, pp. 163–168.
- [20] A. Ibsch, S. Stümper, H. Altinger, M. Neuhausen, M. Tschentscher, M. Schlipfing, J. Salinen, and A. Knoll, "Towards autonomous driving in a parking garage: Vehicle localization and tracking using environment-embedded LIDAR sensors," in *Proc. IEEE Intell. Vehicles Symp. (IV)*, Jun. 2013, pp. 829–834.
- [21] A. Tarko, M. Romero, K. Ariyur, V. Bandaru, and C. Lizarazo, "Detecting and tracking vehicles, pedestrians, and bicyclists at intersections with a stationary LiDAR," in *Proc. 18th Int. Conf. Road Safety Five Continents (RS5C)*, Jeju Island, South Korea, May 2018, pp. 16–18.
- [22] H. Lee and B. Coifman, "Side-fire lidar-based vehicle classification," *Transp. Res. Rec.*, vol. 2308, no. 1, pp. 173–183, Jan. 2012.
- [23] Z. Y. Zhang, J. Y. Zheng, X. Wang, and X. Fan, "Background filtering and vehicle detection with roadside lidar based on point association," in *Proc. 37th Chinese Control Conf. (CCC)*, Jul. 2018, pp. 7938–7943.
- [24] J. Wu, H. Xu, Y. Sun, J. Zheng, and R. Yue, "Automatic background filtering method for roadside LiDAR data," *Transp. Res. Rec.*, vol. 2672, no. 45, pp. 106–114, Jun. 2018.
- [25] J. Wu, H. Xu, Y. Zheng, and Z. Tian, "A novel method of vehicle-pedestrian near-crash identification with roadside LiDAR data," *Accident Anal. Prevention*, vol. 121, pp. 238–249, Dec. 2018.
- [26] J. Zhao, H. Xu, J. Wu, Y. Zheng, and H. C. Liu, "Trajectory tracking and prediction of pedestrian's crossing intention using roadside LiDAR," *IET Intell. Transp. Syst.*, vol. 13, no. 5, pp. 789–795, May 2018.
- [27] Y. Zheng, H. Xu, Z. Tian, and J. Wu, "Design and implementation of the DSRC-bluetooth communication and mobile application with LiDAR sensor," in *Proc. Transp. Res. Board 97th Annu. Meeting*, Washington, DC, USA, Jan. 2018.
- [28] J. Wu, H. Xu, and J. Zhao, "Automatic lane identification using the roadside LiDAR sensors," *IEEE Intell. Transp. Syst. Mag.*, to be published. doi: 10.1109/MITS.2018.2876559.
- [29] J. Wu, H. Xu, J. Zhao, and N. Simpson, "Autonomous wildlife crossing detection method with roadside lidar sensors," in *Proc. Transp. Res. Board 97th Annu. Meeting*, Washington, DC, USA, Jan. 2018.
- [30] J. Zhao, H. Xu, D. Wu, and H. Liu, "An Artificial Neural Network to Identify Pedestrians and Vehicles from Roadside 360-Degree LiDAR Data," in *Proc. Transp. Res. Board 97th Annu. Meeting*, Washington, DC, USA, 2018.
- [31] J. Wu, H. Xu, and W. Liu, "Points Registration for Roadside LiDAR Sensors," *Transp. Res. Rec.*, to be published. doi: 10.1177/0361198119843855.
- [32] J. Wu, H. Xu, B. Lv, R. Yue, and Y. Li, "Automatic ground points identification method for roadside LiDAR data," *Transp. Res. Rec.*, to be published. doi: 10.1177/0361198119843869.
- [33] J. Zhao, H. Xu, H. Liu, J. Wu, Y. Zheng, and D. Wu, "Detection and tracking of pedestrians and vehicles using roadside LiDAR sensors," *Transp. Res. C, Emerg. Technol.*, vol. 100, pp. 68–87, Mar. 2019.
- [34] C. M. Martinez, X. Hu, D. Cao, E. Velenis, B. Gao, and M. Wellers, "Energy management in plug-in hybrid electric vehicles: Recent progress and a connected vehicles perspective," *IEEE Trans. Veh. Technol.*, vol. 66, no. 6, pp. 4534–4549, Jun. 2017.
- [35] L. E. Y. Mimbela and L. A. Klein. (2000). *Summary of Vehicle Detection and Surveillance Technologies Used in Intelligent Transportation Systems*. [Online]. Available: <http://www.fhwa.dot.gov/ohim/tvtw/vdstits.pdf>
- [36] J. Wu and H. Xu, "The influence of road familiarity on distracted driving activities and driving operation using naturalistic driving study data," *Transp. Res. F, Traffic Psychol. Behav.*, vol. 52, pp. 75–85, Jan. 2018.
- [37] M. Lange and J. Detlefsen, "94 GHz three-dimensional imaging radar sensor for autonomous vehicles," *IEEE Trans. Microw. Theory Techn.*, vol. 39, no. 5, pp. 819–827, May 1991.
- [38] P. Fernandes and U. Nunes, "Platooning with IVC-enabled autonomous vehicles: Strategies to mitigate communication delays, improve safety and traffic flow," *IEEE Trans. Intell. Transp. Syst.*, vol. 13, no. 1, pp. 91–106, Mar. 2012.
- [39] A. Talebpoor and H. S. Mahmassani, "Influence of connected and autonomous vehicles on traffic flow stability and throughput," *Transp. Res. C, Emerg. Technol.*, vol. 71, pp. 143–163, Oct. 2016.
- [40] Z. Sun, G. Bebis, and R. Miller, "On-road vehicle detection: A review," *IEEE Trans. Pattern Anal. Mach. Intell.*, vol. 28, no. 5, pp. 694–711, May 2006.
- [41] A. Mukhtar, L. Xia, and T. B. Tang, "Vehicle detection techniques for collision avoidance systems: A review," *IEEE Trans. Intell. Transp. Syst.*, vol. 16, no. 5, pp. 2318–2338, Oct. 2015.
- [42] A. P. Tarko, K. B. Ariyur, M. Romero, V. K. Bandaru, and C. L. Jimenez, "Guaranteed LiDAR-aided multi-object tracking at road intersections," Purdue Univ., Tech. Rep. NEXTRANS Project 145PUY2.2, 2016.
- [43] D. P. Huttenlocher, G. A. Klanderman, and W. J. Rucklidge, "Comparing images using the Hausdorff distance," *IEEE Trans. Pattern Anal. Mach. Intell.*, vol. 15, no. 9, pp. 850–863, Sep. 1993.
- [44] M. Aly, "Real time detection of lane markers in urban streets," in *Proc. IEEE Intell. Vehicles Symp.*, Jun. 2008, pp. 7–12.
- [45] H. Senaratne, M. Mueller, M. Behrisch, F. Lalanne, J. Bustos-Jiménez, J. Schneidewind, D. Keim, and T. Schreck, "Urban mobility analysis with mobile network data: A visual analytics approach," *IEEE Trans. Intell. Transp. Syst.*, vol. 19, no. 5, pp. 1537–1546, May 2018.
- [46] T. Wang, J. Xin, and N. Zheng, "A method integrating human visual attention and consciousness of radar and vision fusion for autonomous vehicle navigation," in *Proc. 4th IEEE Int. Conf. Space Mission Challenges Inf. Technol. (SMC-IT)*, Aug. 2011, pp. 192–197.

...